Environmental Science Nano

ROYAL SOCIETY OF CHEMISTRY

PAPER

View Article Online
View Journal | View Issue

Cite this: *Environ. Sci.: Nano*, 2026, **13**, 1948

Polystyrene nanoplastic exposure promotes amyloid misfolding and metabolic impairment at sublethal doses. A subcellular infrared imaging study

Iran Augusto Neves da Silva, *[abcde] Agnes Paulus,[ac] Valeriia Skoryk,[ace] Kar-Yan Su,[ac] Fátima Herranz-Trillo[e] and Oxana Klementieva*[ac]

Received 18th December 2025,
Accepted 9th March 2026

DOI: 10.1039/d5en01181g

rsc.li/es-nano

Microplastics and nanoplastics (MNPs) are ubiquitous environmental pollutants with increasing implications for human health. While their presence in human tissues is established, the molecular mechanisms driving their potential neurotoxicity remain unclear. This study investigates the impact of polystyrene (PS) on amyloid protein misfolding and cellular metabolism using optical photothermal infrared (O-PTIR) spectroscopy, a label-free, sub-diffraction imaging technique. Our results reveal that PS exposure promotes pathological protein misfolding, specifically decreasing β-sheet-rich conformations, and disrupts metabolic homeostasis at sublethal doses. These suggest that the nanoplastic surface acts as a catalytic scaffold for amyloid aggregation, driving cellular dysfunction prior to acute toxicity. This identifies a plausible molecular pathway by which environmental MNP pollution contributes to the risk and progression of neurodegenerative diseases, highlighting the need for risk assessments that look beyond simple cell survival.

Environmental significance

The potential for environmental micro- and nanoplastics (MNPs) to bioaccumulate in the human brain is a growing global concern, yet the specific molecular pathways linking this exposure to neurodegeneration remain undefined. This study demonstrates that polystyrene nanoplastics are not biologically inert but act as catalytic scaffolds that promote pathological protein misfolding. Critically, we show that these nanoscale structural alterations occur at sublethal doses where standard cytotoxicity assays show no alarm. This identifies a significant "blind spot" in current environmental risk assessments: plastic pollution may drive chronic neurodegenerative processes (like amyloidosis) long before causing acute cellular toxicity. These findings provide a mechanistic basis for the link between environmental pollution and Alzheimer's disease, urging a shift in toxicological screening from simple cell survival to molecular conformational integrity.

Introduction

Microplastics (MPs, <5 mm) and nanoplastics (NPs, defined as particles smaller than 1 μm (<1000 nm)), collectively referred to as MNPs, are pervasive pollutants found in air, soil, food packages, and water.[1,2] Polystyrene (PS), specifically, is a critical priority for toxicological assessment, as it is one of the six most abundant plastic polymers, accounting for a significant portion of global plastic production.[3]

Human exposure to MNPs is pervasive and occurs through multiple pathways, including ingestion, inhalation, and dermal absorption.[4–6] Sources include everyday items like food containers, which unintentionally release MPs into the body. High-temperature exposure, such as when drinking hot beverages, can significantly increase the release of billions of microparticles and nanoparticles from sources like plastic teabags and paper cups.[7] This high environmental mobility and bioaccessibility has led to general health concerns, including endocrine disruption, reproductive toxicity, and cancer.[6,8]

MNPs can cross biological barriers, potentially accumulating in the brain, which may lead to cognitive issues.[1] Recently, MNPs were detected to bioaccumulate in human brain tissue.[9] These findings raise critical concerns

[a] *Medical Microspectroscopy, Department of Experimental Medicine, Faculty of Medicine, Lund University, Sölvegatan 19, BMC, B10, 221 84 Lund, Sweden. E-mail: iran.augusto_silva@med.lu.se, oxana.klementieva@med.lu.se*
[b] *Lund Stem Cell Center, Faculty of Medicine, Lund University, Lund, Sweden*
[c] *NanoLund, Lund University, Lund, Sweden*
[d] *Wallenberg Center for Molecular Medicine, Faculty of Medicine, Lund University, Lund, Sweden*
[e] *MAX-IV Laboratory, Lund, Sweden*

that environmental contaminants may exacerbate the molecular pathologies underlying neurodegenerative conditions, such as Alzheimer's disease (AD).

AD is a progressive neurodegenerative disorder characterized by memory loss, cognitive decline, and neuronal death. It is pathologically defined by the accumulation of extracellular amyloid plaques and intracellular neurofibrillary tangles.[10] While the exact cause of AD remains multifactorial, the potential for environmental pollutants to trigger surface-catalysed amyloid aggregation is a growing concern. Research indicates that polystyrene can modulate the formation of amyloid fibrils, with studies showing that particles around 400 nm significantly promote the primary nucleation step in proteins like hen egg-white lysozyme (HEWL).[2] This effect is attributed to hydrophobic interactions occurring at the interface and junction of the protein corona that forms around the polystyrene particles.[11,12] Notably, mechanistic studies utilizing elevated exposure models have successfully demonstrated that MNPs can induce oxidative injury and neuronal apoptosis in fetal thalamus and neuronal cell lines.

Recent studies have begun to elucidate the specific role of the 'protein corona' in neurodegeneration. For instance, Wang *et al.* demonstrated that nanoplastics can perturb metabolic processes through nano–bio interface interactions,[13] while Liang *et al.* reported plastic-associated protein misfolding in neurodegenerative disease contexts.[14] Similarly, *in vitro* studies by Bashirova *et al.* and Gou *et al.* have shown that PET and polystyrene nanoplastics can accelerate amyloid fibril formation and alter secondary structures.[15,16] However, these investigations have largely relied on bulk assays or conventional imaging, which lack the spatial resolution to correlate specific chemical structural changes with subcellular localization *in situ*. Consequently, a significant knowledge gap remains in visualizing the precise chemical 'fingerprint' of these misfolded species within the crowded cellular environment at sub-diffraction resolution.

MNPs also interfere with lipid metabolism, potentially causing the accumulation of toxic lipid species in the brain[1,2] and contributing to neuronal dysfunction.[17–20] Additionally, MNPs not only bind to lipids, altering their structure and function, but also induce broader cellular damage, including inflammation and cell death.[21] Despite growing concerns, the exact mechanisms by which MNPs contribute to AD processes remain poorly understood.[22,23]

In AD, amyloid beta (Aβ) peptides misfold and aggregate into a range of structural forms, from soluble oligomers to insoluble fibrils, which typically accumulate extracellularly to form amyloid plaques.[24] However, growing evidence indicates that intracellular aggregation and the structural conformation of Aβ particularly oligomeric β-sheet-rich species are more closely associated with neurotoxicity.[25]

This study investigates whether nanoplastic exposure, specifically to PS, influences the intracellular aggregation of Aβ. We hypothesize that PS promotes conformational changes such as the formation of β-sheet-rich structures and oligomeric species that disrupt cellular homeostasis. To model this, we used N2A cells overexpressing human amyloid precursor protein (APP) carrying the Swedish mutation (N2Aswe).

To further delineate whether the observed structural alterations arise from direct surface-mediated interactions or secondary intracellular processes, we complemented the cellular studies with controlled experiments using synthetic Aβ(1–42) incubated with polystyrene particles. This reductionist approach enabled direct assessment of surface-driven conformational remodelling independent of cellular metabolism. By integrating sub-diffraction O-PTIR imaging in cells with spectroscopic analysis of purified protein, the study bridges bulk biophysical observations and spatially resolved intracellular structural mapping, providing mechanistic insight into how polystyrene surfaces modulate amyloid folding pathways. O-PTIR combines the molecular specificity of infrared (IR) absorption with the spatial resolution of visible light, overcoming the diffraction limits of conventional IR techniques to achieve submicron resolution (~500 nm).[26] The amide I region (1600–1700 cm^{-1}), which reflects the C═O stretching vibrations of peptide bonds, is particularly informative for detecting structural transitions of proteins.[27,28]

Within the amide I region (1600–1700 cm^{-1}), several sub-bands are particularly informative for amyloid research. β-sheet structures typically show strong absorption in the lower range (~1610–1640 cm^{-1}), with aggregated or intermolecular β-sheets appearing around 1610–1625 cm^{-1}. Native antiparallel β-sheets are observed near 1625–1640 cm^{-1}, while a high-frequency component around 1680–1695 cm^{-1} also corresponds to β-sheet structures. In contrast, α-helices and random coils appear at higher wavenumbers (~1640–1658 cm^{-1} and ~1640–1650 cm^{-1}, respectively) and turns or loops are usually detected in the 1660–1680 cm^{-1} range. The ratio of these spectral features enables the discrimination of different amyloid conformations and aggregation states *in situ*.[29,30]

Our results provide direct mechanistic evidence that PS exposure drives pathological protein misfolding, specifically evidenced by a distinct shift toward β-sheet-rich conformations, with decreased unordered and antiparallel β-sheets detected at ~1640 cm^{-1} and 1694 cm^{-1}, respectively. Beyond structural alterations, PS exposure severely disrupted metabolic homeostasis, demonstrated by a substantial decrease in metabolic activity and lysosomal dysfunction. These critical findings, obtained through the subcellular resolution of O-PTIR, confirm that the nanoplastic surface acts as a catalytic scaffold for amyloid aggregation. This identifies a plausible molecular pathway by which environmental plastic pollution contributes to the etiology of neurodegenerative diseases, highlighting an urgent need to reassess the chronic health risks of MNP accumulation in the brain.

Materials and methods

Commercially available labelled 365/415 nm (DAPI) and 580/605 nm (CY5) PS beads, FluoSpheres carboxylate-modified microspheres with a diameter of 0.2 μm, were obtained from Thermo Fisher (cat. F8805 and F8810 with a concentration of 2% solids in 10 ml solution). The 200 nm size was selected to model the nanoplastic fraction (<1 μm) because it falls within the optimal size range for efficient cellular internalization *via* endocytic pathways.

Cell culture and exposure

N2A cells (ATCC CCL-131) were utilized in this study. Two variants were prepared: the N2A wild type (N2Awt), representing the non-transfected parental cell line, and the N2A cell line stably transfected with human APP carrying the Swedish mutation[31] (N2A APPSwe), which will be referred to as N2Aswe in further experiments. Both N2Awt and N2Aswe cells were cultured in a 1:1 ratio of DMEM and Opti-MEM (31985062; Gibco), supplemented with 10% FBS and 1% penicillin/streptomycin, and maintained at 37 °C with 5% CO_2. N2Aswe cells were selected for stable expression using 50 mg ml^{-1} geneticin (10131027; Gibco) in their media. For experimental procedures, cells were exposed to PS concentrations of 0, 120, 240, and 480 μg mL^{-1}. These concentrations were selected to align with recent mechanistic investigations into PS-induced neurotoxicity and ROS-mediated injury, ensuring a comparable toxicological baseline for evaluating surface-catalysed protein misfolding[32] and Aβ(1–42) for either 24 or 48 h once they reached 60% confluence. For correlative O-PTIR imaging (Fig. 4), N2Awt cells were seeded on CaF_2 windows and treated for 24 h with either 10 mM Aβ(1–42) alone, PS nanoplastics alone (480 μg mL^{-1}), or a co-exposure of both.

Metabolic assessment of N2Aswe WST-1

Metabolic activity (*i.e.*, cell viability) was assessed using the water-soluble and cell-permeable tetrazolium salt reagent (WST-1), which is reduced on the membrane of mitochondria in living cells.[33] Following intracellular cleavage of WST-1 by cellular mitochondrial dehydrogenases into formazan, the cell-permeable formazan is released into the cell culture medium and can subsequently be measured by removing the liquid and reading it in a standard UV-vis plate reader. Absorbance can be viewed as proportional to the metabolic activity of living cells. Therefore, lower amounts of formazan indicate a reduced metabolic activity. N2Aswe cells exposed to (0, 120, 240 and 480 μg ml^{-1}) for 24 and 48 h were incubated with 90 μL of complete medium and 10 μL of WST-1 (Roche, Sigma-Aldrich, USA) for 1 h at 37 °C in a humidified incubator with 5% CO_2. Supernatant optical density was measured at 440 and 650 nm on an Epoch plate reader (BioTek, Winooski, VT, USA). 440 nm wavelength was used as a representative for the specific conversion of WST-1 by metabolically active cells, and 650 nm was used as a reference wavelength for nonspecific absorbance. Complete medium without tissue served as a negative control. All assays were performed in independent biological triplicate (n = 3).

Lactate dehydrogenase assay

To assess the cytotoxic effect of polystyrene (PS) and Aβ(1–42) exposure, a lactate dehydrogenase (LDH) cytotoxicity detection kit (ab197004, Abcam, Cambridge, UK) was used. Monomeric Aβ(1–42) was prepared from a stock solution of 250 mM in DMSO. The peptide was diluted in culture medium immediately prior to use to ensure it remained in its monomeric state for the duration of the 24-h exposure. Both N2Awt and N2Aswe cells were cultured for 24 h prior to exposure, with treatments conducted for an additional 24 h. All conditions were performed in triplicate (n = 3). The experimental groups were PS dose response (0 (untreated control), 100, 120, 240, and 480 μg mL^{-1} PS), Aβ (10 mM Aβ(1–42) in the medium), and a co-exposure group (480 μg mL^{-1} PS combined with 10 mM Aβ(1–42)). Following the 24-h exposure, approximately 5 μL of supernatant from each treatment group were collected. The LDH reaction mix solution (95 μL) was prepared by combining 2 μL of developer mix I/LDH substrate mix, 4 μL of Pico Probe III/Pico Probe, and 89 μL of LDH assay buffer. 95 μL of the prepared LDH reaction mix solution was added to 5 μL of the collected supernatant in a 96-well plate. The plate was then incubated at room temperature in the dark for 10 min. Controls included background control (basal medium only), negative control (untreated cell supernatant), lysate control (supernatant from lysis buffer-treated cells, representing maximum release), and a positive control (LDH positive control buffer provided by Abcam). Fluorescence was measured at an excitation/emission wavelength of 535 nm/587 nm using a Cytation 5 Cell Imaging Multi-Mode Reader. Data are reported in relative fluorescence units (RFUs), calculated as per the manufacturer's suggested protocol and normalized against the background media control. The percentage of cytotoxicity was calculated by normalizing the LDH release of the exposed samples against the maximum release (lysate control).

Optical photothermal infrared spectroscopy

For microspectroscopy we used the mIRage system (Photothermal Spectroscopy Corp., Santa Barbara, CA, USA) at Lund University within the Integrated Vibration Spectroscopy-Microsom Laboratory for Molecular-Scale Biogeochemical Research. The IR source was a pulsed, tunable four-stage quantum cascade laser (QCL) operating in the IR with a repetition rate of 100 kHz, inducing localized heating and thermal expansion in the sample. This photothermal expansion in the sample was detected using a 532 nm green probe laser, enabling the acquisition of quantitative absorption spectra. Background spectra were collected on a built-in reference sample. Further details about the method can be found in ref. 34–38. For the experiment

investigating Aβ fibrillization induced by PS, the following instrument settings were applied. Single spectra were collected within the 1300 cm^{-1} to 1800 cm^{-1} range using a standard silicon photodiode detector with a gain of 50×. The IR power was set to 100% and the probe power to 4.7% with an average of 10 spectra. Background spectra were obtained from a built-in reference standard to ensure consistency and calibration across measurements. The IR spectra were cut to the amide I region, spanning 1500–1700 cm^{-1}.

Data analysis

The spectra obtained from the experiments were analysed using Quasar-M data mining software.[39] A linear baseline correction was applied to remove any systematic offset. The spectra were then vector-normalized to correct for variations in overall signal intensity. To enhance the number of discriminative spectral features, the Savitzky–Golay smoothing algorithm was used, implemented with a 13-point window and a second-order polynomial. For the analysis of N2Awt cells exposed to exogenous Aβ(1–42) and PS (Fig. 4), O-PTIR ratio maps were generated using the specific wavenumbers for β-sheet structures (1632/1655 cm^{-1}) and PS (1494/1350 cm^{-1}) to evaluate their spatial colocalization. To examine the impact of PS on N2Aswe cells, high-resolution hyperspectral maps were collected using an APD detector with a spatial resolution of 0.5 μm × 0.5 μm from individual cells (5 cells non-exposed and 6 cells exposed to PS) selected from n = 3 independent biological replicates across the spectral range of 1000 cm^{-1} to 1750 cm^{-1}. For each cell, between 370 and 400 spectra were acquired. The IR source power was set to 58%, the probe power to 0.5%, and 5 spectra were averaged per measurement. For the analysis, to focus on the region associated with protein secondary structure, the spectra were cut to the 1610–1710 cm^{-1} range (amide I). To enhance spectral features and resolve overlapping peaks relevant to structural protein analysis, spectra were processed by calculating the second-order derivative of each spectrum using the Savitzky–Golay algorithm with a 7-point window. To ensure data quality and robustness for all the collected spectra for the experiments, an unsupervised outlier detection method was applied. Approximately 10% of the spectra identified as anomalous were excluded using the LOF algorithm.

In order to analyse the intensity ratios, the total β-sheet content was determined by calculating the intensity ratio (Table 1) between 1630 cm^{-1} (attributed to β-sheet structures) and 1658 cm^{-1} (to the total protein/α-helices peak). Spectral components associated with antiparallel β-sheet structures (~1694 cm^{-1}) were quantified by their intensity ratio relative to both total proteins (~1658 cm^{-1}) and total β-sheet structures (~1630 cm^{-1}). Similarly, components indicative of unordered β-sheet structures (~1640 cm^{-1}) were calculated based on their intensity ratio relative to total proteins (~1658 cm^{-1}) and total β-sheet structures (~1630 cm^{-1}). These specific IR peaks were selected based on established spectral assignments in the literature.[40] Principal component analysis (PCA) was used to explore differences in the IR spectral profiles of N2Aswe cells exposed to PS compared to non-exposed controls. Prior to PCA, spectra were processed by calculating the second derivative, followed by baseline correction and normalization to the total protein peak at 1658 cm^{-1}. PCA was performed on the 1610–1710 cm^{-1} region corresponding to amide I vibrations. Components were retained based on the screen plot and cumulative explained variance, with the first four components accounting for 70% of the total variance. PCA scatter and loading plots were used to assess group separation and identify spectral features contributing to observed differences. All analyses were conducted on the pre-processed dataset, enabling reproducible and reliable comparisons across experimental conditions.

Table 1 Infrared band positions and their assignments to biomolecular vibrational modes[29,30,41–44]

Band position (cm^{-1})	Vibrational assignments, ν
1602	Polystyrene; aromatic ring
1630	Major β-sheets; amide I
1640	Random coil/unordered structures; amide I
1658	α-Helices in proteins; amide I
1694	Minor antiparallel β-sheets; amide I

ν – stretching mode.

Electron microscopy

Transmission electron microscopy (TEM). After 1 h of aggregation, we placed a droplet of the PS + Aβ(1–42) mixture onto a 400-mesh, 3 mm copper grid with a carbon support film (EM Resolutions Ltd., Sheffield, UK) and let it incubate for 10 min. We then quickly washed the grid twice with Milli-Q water and left it to air dry until imaging. Imaging was performed on a JEOL 1400Plus (120 kV) instrument.

Scanning electron microscopy (SEM). For SEM analysis, individual samples of diluted PS, diluted Aβ(1–42), and the combined PS + Aβ(1–42) mixture were prepared. Five microliters of each sample were deposited onto separate silicon wafers and air-dried completely. Prior to imaging, dried samples were sputter-coated with a thin layer of gold for enhanced conductivity. SEM imaging was carried out using a Hitachi SU3500 electron microscope at the Microscopy Platform at the Department of Biology, with images acquired at an accelerating voltage of 5 kV and a working distance of 5470 μm.

Fluorescence labelling. According to the manufacturer's protocol, Amytracker® 520 (Ebba Biotech, Solna, Sweden) was diluted from 1 : 1000 in the presence of DAPI diluted from 1 : 10 000, and living tissue slices were incubated for 30 min at room temperature in a 24-well plate. 82E1 primary antibody (IBL, 1 : 1000 dilution) was used to detect total Aβ, Ab-42 antibody conjugated with 555 Alexa (1 : 1000), while OC78 (Abcam, 1 : 1000 dilution) primary antibody was applied

to detect fibrillar oligomeric forms including soluble oligomeric forms. Cells were incubated with Alexa 568 goat anti-mouse and Alexa 648 goat anti-rabbit antibody (dilution 1 : 1000) for 1 h and then mounted with DAKO mounting medium for observation. The primary antibodies used were LAMP1 (Abcam, 1 : 2000 dilution) as an indicator of lysosome formation, where PS particles were expected to accumulate, and anti-caspase-3 (Cell Signalling Technologies, 1 : 1000 dilution) as an apoptotic marker. Amytracker 630 (Ebba Biotech, cat. number: A630-50EX, 1 : 1000 dilution) was also used to potentially detect amyloid accumulation. Cells were then incubated with Alexa 488 goat anti-rabbit (Invitrogen, cat. number: A11034) and Alexa 568 goat anti-rat antibody (Invitrogen, cat. number: A11077) at a dilution of 1 : 1000. Imaging was done using a BioTek Cytation 5 Cell Imaging Multi-Mode Reader and an epifluorescence Axio Zeiss microscope system. PBS–Tween 20 was used as a washing buffer for the immunofluorescence, and 1% BSA in 1× PBST acted as both blocked buffer and antibody dilution buffer.

Small-angle X-ray scattering. Small-angle X-ray scattering (SAXS) measurements were performed to determine the radius of gyration (R_g) of PS both alone and in the presence of (Aβ(1–42)) in physiological buffer at room temperature. All samples were carried out at CoSAXS beamline at the synchrotron facility MAXIV (Lund, Sweden), operated at a fixed energy (12.4 keV, λ = 0.99 Å) with an incident X-ray beam focused on the detector. The sample-to-detector (Eiger2 X 4M) distance was set at 10 m, yielding a q-range of $0.0033 < q < 0.26$ Å^{-1}, suitable for analysing PS diameter. The scattering intensity was recorded as a function of the scattering vector (q), and the data were processed to extract R_g values using the Guinier approximation.[45,46] The final concentration of PS and Aβ(1–42) in the mixtures was adjusted to 2 mg ml^{-1} and 0.04 mg ml^{-1}, respectively. The concentration of monomeric Aβ(1–42) was set below the detection limit to exclude contribution to scattering. Buffer-only controls were subtracted from all datasets to eliminate background contributions.

Imaging. Imaging was acquired using the manual mode in a Cytation 5 multimode reader (Agilent Technologies, USA). Montage images were collected at 4× magnification. Bright-field and DAPI imaging filter cubes were used with the following acquisition settings: bright-field: LED intensity: 10, integration time: 21, camera gain: 24, immunofluorescence. DAPI: LED intensity: 4, integration time: 5, camera gain: 1. GFP: LED intensity: 3, integration time: 98 camera gain: 18. TEXAS: LED intensity: 6, integration time: 528 and camera gain: 18. CY5 LED intensity: 2, integration time: 1994 and camera gain: 18, DAPI: LED intensity: 8, integration time: 5, camera gain: 1. Immunofluorescence images were acquired using a Zeiss Axio Imager microscope (Zeiss Axio Imager M2) where images were collected at 40× magnification and used afterwards for the fluorescence intensity calculation of the specific antibodies mentioned above. At least eight images per group were collected. Quantitative analysis of the area and intensity of specific fluorescence signals was performed using FIJI software, with group comparisons made using the Mann–Whitney U-test.

Results

To determine if O-PTIR could effectively investigate PS in a label-free setting and under various conditions, we first evaluated its ability to analyse the spectral absorption characteristics of PS on CaF_2 substrates. Our analysis identified distinct spectral markers at 1600 cm^{-1}, 1494 cm^{-1}, 1453 cm^{-1}, and 1027 cm^{-1} for PS, which could serve as references for future experiments. These markers are consistent with previous literature (Fig. 1).[44,47,48]

Aβ fibrillization induced by the presence of PS

To investigate how PS nanoplastics influence amyloid protein structure, we incubated recombinant Aβ(1–42) with PS for 1 h. Fig. 2A provides a schematic overview of the experimental timeline, illustrating the separate observation of PS and Aβ and their co-incubation over time. Fluorescence microscopy, presented in Fig. 2B, demonstrates the impact of PS on Aβ(1–42) aggregation. Initially, Aβ(1–42) alone appeared as smaller structures. At time zero (T_0) of co-incubation, PS and Aβ(1–42) showed some initial aggregates, with a significant increase in aggregate size and fluorescence intensity observed after 1 h of co-exposure. The accompanying graph in Fig. 2B.i quantifies this observation, showing a significant increase in Aβ fluorescence size when co-incubated with PS, both at T_0 and after 1 h, compared to Aβ alone.

Further, corroborating the fluorescence microscopy data, transmission electron microscopy (TEM) and scanning electron microscopy (SEM) images in Fig. 2C provide detailed ultrastructural insights. TEM images confirmed the approximately 200 nm size of individual PS particles. At T_0 of the PS + Aβ(1–42) co-incubation, TEM revealed the early formation of aggregates. After 1 h, these evolved into distinct larger structures resembling amorphous protofibrils,

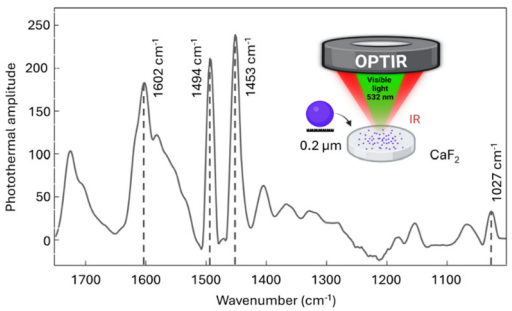

Fig. 1 O-PTIR spectra of PS. The inset shows the principle of how O-PTIR operates: an IR laser is used to induce photothermal expansion within the sample, while green laser (532 nm) is used to probe the localized thermal effect. These specific absorption bands are consistent with previously reported literature.[44,47,48] O-PTIR schematics created in BioRender, Silva, I. (2025) (https://BioRender.com/d94r687).[66]

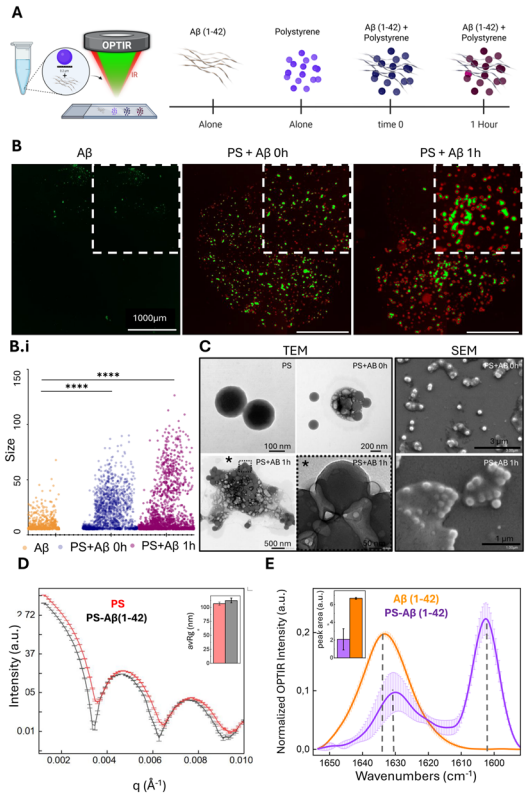

Fig. 2 Characterization of the PS interaction with Aβ(1–42). (A) The experimental timeline is schematically created in BioRender, Silva, I. (2025) (https://BioRender.com/sc8onrp).[67] (B) Immunofluorescence imaging displays Aβ(1–42) in green and PS in red. (B.i) Adjacent to the images, a graph depicts the increase in aggregation from Aβ(1–42) alone to the PS + Aβ(1–42) combination at T_0 and after 1 h (scale bar: 1000 μm). (C) TEM/SEM representative images of PS alone, Aβ(1–42) alone, to the PS + Aβ(1–42) at T_0 and after 1 h. (D) SAXS plot demonstrating changes in the average area of PS alone and PS + Aβ combination. Inset: Comparison of the calculated radius of gyration (R_g) for both samples. (E) O-PTIR spectra of Aβ(1–42) alone and PS + Aβ(1–42) after 1 h (data representative of 3 independent experiments). Inset: Quantification of β-sheet content by calculating the integrated area of the ~1632 cm^{-1} peak.

consistent with early-stage aggregation, rather than mature long fibrils. Final confirmation of aggregation and area increase was obtained from SAXS experiments (Fig. 2D), which compared the average area of PS alone to that of the PS + Aβ(1–42) combination. This analysis demonstrated that the PS + Aβ(1–42) mixture formed significantly larger structures, with a radius of gyration of 112.1 ± 3.9 nm as compared to PS alone with a radius of gyration of 106.7 ± 2.7 nm. Finally, O-PTIR spectroscopy provided crucial molecular-level insights directly supporting Aβ(1–42) fibrillization induced by the presence of PS. To quantify structural changes during early aggregation, we calculated the integrated area of the β-sheet-associated band at 1630 cm^{-1}. The peak area for isolated Aβ(1–42) increased from 2.08 ± 1.19 at time 0 to 6.66 ± 0.08 after 1 h of incubation, indicating a clear enrichment of β-sheet structures during early aggregation. This observation is consistent with the progressive structural transition of Aβ toward β-sheet-rich assemblies. Fig. 2E demonstrates O-PTIR spectra highlighting specific wavenumber characteristic of both PS and Aβ(1–42), revealing the spectral interplay upon their co-incubation and indicating structural modifications due to their interaction. Specifically, the characteristic peak for PS at ~1600 cm^{-1} (also seen in Fig. 1) and the Aβ(1–42) peak at ~1632 cm^{-1} are clearly observed in the same sample after 1 h of co-exposure, confirming their spatial co-localization within the aggregates. The area under 1632 cm^{-1} peak was 2.08 ± 1.19 at time 0 and increased to 6.66 ± 0.08 after 1 h of incubation for pure Aβ, consistent with the expected increase in β-sheet content. This allowed us to compare amyloid structures formed by pure Aβ(1–42) and PS-bound Aβ(1–42). A notable strength of O-PTIR is its capacity to identify these interactions from the initial time point (0 h) to 1 h, enabling differentiation of individual materials at 0 h and subsequent tracking of the specific region for mapping or future analysis in the same area of their co-presence after exposure. The full spectral data, demonstrating the interrelation and progression across all four conditions (Aβ(1–42) alone, PS alone, Aβ(1–42) + PS at T_0, and Aβ(1–42) + PS after 1 h) can be seen in Fig. S1.

Dose-dependent cytotoxicity and metabolic impact of PS on cells

Subsequently, we explored PS interaction in a more complex system. We conducted experiments on PS incorporated into N2Aswe cells, which increased the sample complexity while providing a well-defined and controlled environment. The experiments were performed with PS of a spherical shape, with an average diameter of 0.2 μm. Details on the PS and sample preparation are described in the Materials and methods section. We aimed to determine the optimal dose and exposure time to evaluate the effects of PS on cellular metabolism. To do this, we conducted two sets of experiments. Cells were analysed after 24 and 48 h (Fig. S2). These findings help us evaluate the extent of changes and determine whether a 24- or 48-h exposure is more appropriate for subsequent experiments.

To assess cellular uptake and cytotoxicity, we exposed cells to various concentrations of PS (0, 120, 240, and 480 μg ml^{-1}) for 24 and 48 h. Bright-field microscopy (Fig. S2A) revealed the uptake of PS by cells, visualized as yellow-highlighted regions indicating increased PS dose, and which also increases the fluorescence intensity.

To quantify the impact of PS on cell viability, we performed a WST-1 assay (Fig. S2B). We found a clear correlation between PS bead exposure and impaired cellular function. The WST-1 assay revealed a significant decrease in metabolic activity at all tested concentrations, suggesting PS-induced cytotoxicity.

Cytotoxicity validation by LDH assay

To definitively validate whether the observed metabolic impairment correlated with cellular damage or cell death, we performed the LDH cytotoxicity assay across the 24 h exposure time-point (Fig. S2C). This assay directly measures LDH release into the medium, an indicator of plasma membrane integrity loss and irreversible cell death. The

results confirm that the chosen PS concentrations did not induce high levels of cytotoxicity in either the N2Awt or the N2Aswe cells.

Across all tested doses of PS 120 to 480 μg mL^{-1}, LDH release remained comparable to, or only slightly above, that of the untreated control groups, demonstrating that the doses selected for mechanistic study were sublethal and did not cause widespread cell death. Crucially, in N2Awt cells, neither the exposure to 10 mM Aβ(1–42) alone nor the co-exposure of 480 μg mL^{-1} PS + 10 mM Aβ(1–42) resulted in acute cell death. This demonstrates that neither the Aβ(1–42) peptide alone nor its combination with the highest dose of PS is intrinsically cytotoxic at this early stage. In summary, while the WST-1 assay indicates a significant dose-dependent metabolic disturbance, the LDH assay confirms that this effect occurs without inducing severe cell death or overwhelming acute toxicity from the Aβ(1–42)/PS combination, validating the use of these doses for the study of structural and functional changes that precede apoptosis.

Immunofluorescence-based analysis of cell viability loss, lysosomal engagement, and amyloid aggregation in response to PS exposure

To evaluate the impact of PS on cell viability and amyloid-related stress, we analysed immunofluorescence markers for lysosomes (Lamp1), apoptosis (caspase-3), and Aβ different aggregation state (82e1, Aβ42, OC78, Amytracker) (Fig. 3A), followed by (Fig. 3B) providing a signal colocalization assessment plot of the interaction of the markers in the presence of PS.

Lysosomal response and adaptation failure

At 24 h, Lamp1 intensity and area were elevated in both N2Awt (WT) and N2Aswe (SW) cells exposed to PS (Fig. 3E) as well as in non-exposed controls (Fig. S2A), likely reflecting baseline activation after seeding. However, only PS-exposed WT and SW cells showed significant co-localization between Lamp1 and PS (Manders and Pearson, $p < 0.05$), confirming lysosomal uptake of PS particles (Fig. 3C and D).

By 48 h, Lamp1 levels in controls dropped significantly ($p < 0.05$), indicating normal adaptation in the absence of PS. In contrast, N2Awt and N2Aswe cells maintained high Lamp1 area and intensity, suggesting sustained lysosomal activity in response to PS exposure. Despite this, Lamp1-PS co-localization (Manders and Pearson) declined significantly in both groups from 24 h to 48 h ($p < 0.05$). The drop was sharper in N2Aswe, pointing to impaired lysosomal processing, likely due to the combined burden of PS and Aβ accumulation.

These results suggest that while both N2Awt and N2Aswe cells initially respond to PS *via* lysosomal engagement, N2Aswe cells fail to adapt by 48 h, consistent with lysosomal dysfunction or degradation. The more pronounced Pearson decrease in N2Aswe cells supports the interpretation that PS–Aβ complexes are more resistant to clearance, increasing toxicity.

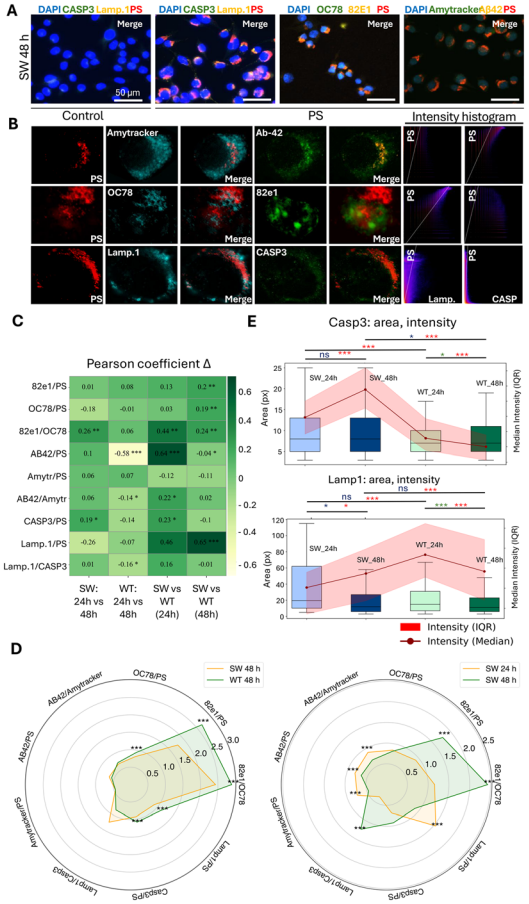

Fig. 3 Cell viability loss, lysosomal engagement, and amyloid aggregation in response to PS exposure in N2Aswe (SW) and N2Awt (WT) cells at 24 h and 48 h. Scale bar: 50 μm. (A) Overview of the immunofluorescence panel used for the analysis of lysosomal (Lamp1), apoptotic (caspase-3 (Casp3)), and Aβ (82e1, Aβ42, OC78, Amytracker) markers with PS particles. (B) Schematic workflow outlining the co-localization analysis process using Pearson and Manders metrics. (C) Pearson correlation coefficients quantifying the degree of spatial overlap between PS and target markers. (D) Manders M1/M2 ratio plots comparing co-localization trends across genotypes and timepoints. (E) 2D histograms showing distribution of positive signal area and intensity for Casp3 and Lamp1 (data derived from n = 8 images per group). Error bars represent SEM.

Apoptosis is triggered by persistent PS and Aβ burden

Caspase-3 intensity increased over time in both genotypes but was significantly higher in N2Aswe cells at 48 h ($p < 0.05$, Fig. 3E). Co-localization with PS was present, but Manders M2 for Casp3–Lamp1 remained low, suggesting that apoptosis occurred near, but not within, lysosomal compartments (Fig. 3D and S3C). This supports the idea that PS aggregates not efficiently cleared by lysosomes initiate apoptotic stress, especially in N2Aswe cells, where Aβ burden exacerbates the effect. N2Awt cells also showed a statistically significant apoptotic response to PS, but to a lesser degree, confirming that PS alone is toxic, while the N2Aswe genotype amplifies the damage.

PS enhances Aβ aggregation, accelerated in SW cells

At 24 h, PS co-localized mainly with monomeric Aβ markers (82E1, Aβ42) in N2Aswe cells. By 48 h, there was a shift toward increased labelling with OC78 which detects fibrillar oligomers and partially covers soluble oligomeric species and Amytracker, which specifically binds mature fibrils as indicated by elevated Manders M1 and Pearson coefficients ($p < 0.05$) (Fig. 3D), indicating amyloid maturation around PS.

N2Awt cells statistically confirmed the trend of amyloid maturation, but with lower magnitude, suggesting that PS can nucleate Aβ aggregation, while N2Aswe cells accelerate the transition toward oligomeric and fibrillar forms associated with increased toxicity.

These findings strongly align with previous observations by Gou *et al.*,[49] who demonstrated that nanoplastics can accelerate Aβ aggregation and potentiate neurotoxicity. PS particles likely act as catalytic surfaces for Aβ oligomerization *via* hydrophobic interactions, leading to increased burden on cellular clearance systems and loss of viability. These findings show that PS exposure induces lysosomal stress, amyloid aggregation, and apoptosis. In N2Aswe cells, the response is more sustained and dysfunctional, likely due to amyloid accumulation overwhelming degradation pathways. Even in N2Awt cells, prolonged PS exposure leads to cellular decline, supporting the hypothesis that PS nanoplastics are intrinsically toxic and exacerbate Aβ pathology when present.

Nanoplastic exposure induces amyloid misfolding independently of endogenous Aβ production

To explore structural changes of Aβ induced by PS in a cellular environment, N2Awt cells were treated for 24 h with 10 mM Aβ(1–42) alone, 480 μg ml^{-1} PS alone, or a combination of Aβ and PS at the corresponding concentrations. In the absence of nanoplastics, Aβ-treated cells exhibited a pronounced shoulder in the amide I region (~1630–1635 cm^{-1}), consistent with β-sheet-rich aggregate formation. Upon addition of nanoplastics, this β-sheet-associated shoulder was markedly reduced, indicating a structural rearrangement of Aβ and a decrease in the relative β-sheet contribution (Fig. 4A). These findings suggest that nanoplastic exposure alters Aβ conformation rather than simply increasing aggregate load.

In both the PS exposed and the Aβ + PS exposed cells, additional characteristic bands attributed to PS were detected at approximately ~1602, 1494, and 1350 cm^{-1}. These peaks co-occurred with protein-associated signals, supporting spatial coexistence of PS and aggregated Aβ. For the subsequent experiment, in which nanoplastics were added to N2Awt cells treated with exogenous Aβ, the 1602 cm^{-1} band was selected for mapping and quantitative analysis. Although the PS-related bands at 1494 and 1350 cm^{-1} were detectable, they exhibited higher noise levels and lower spectral stability (Fig. 4B and C).

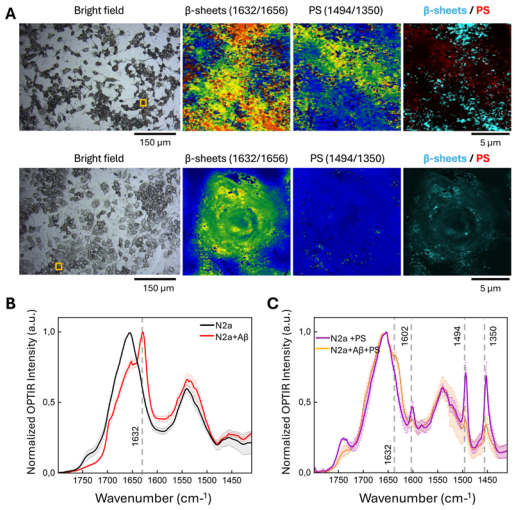

Fig. 4 Correlative O-PTIR imaging and spectral analysis of N2Awt cells exposed to PS nanoplastics and Aβ(1–42). (A) Bright-field images of N2Awt cells following co-exposure to PS and Aβ(1–42) (top) and N2Awt cells, control. The yellow box indicates the region selected for high-resolution O-PTIR analysis. Corresponding O-PTIR ratio maps show the spatial distribution of β-sheet structures (1632/1655 cm^{-1}), PS (1494/1350 cm^{-1}), and their colocalization, revealing heterogeneous protein organization and local structural variations across the treated cell layer. The pseudo-coloured segmentation map (right) highlights β-sheet-enriched regions (cyan) relative to PS (red). (B) Normalized O-PTIR spectra extracted from unexposed N2Awt cells (control) and N2Awt cells exposed to Aβ(1–42). Dashed line indicates characteristic wavenumbers associated with β-sheet structure. (C) Normalized O-PTIR spectra extracted from N2Awt cells exposed to PS alone and from N2Awt cells co-exposed to PS and Aβ(1–42). Dashed lines indicate characteristic wavenumbers associated with β-sheet structure and PS. These bands are detected within the same spectra in N2Awt cells exposed to PS and Aβ(1–42), indicating their co-occurrence within the analyzed regions.

Structural modifications of β-sheets induced by PS *in vitro*

Given that N2Aswe cells overexpress human APP and generate high levels of Aβ providing the necessary substrate to observe pathological misfolding, we focused our high-resolution O-PTIR structural analysis specifically on this AD model. To further investigate the effect of PS on protein structure at the subcellular level, we employed O-PTIR microscopy to assess β-sheet distribution in N2Aswe cells. Hyperspectral maps were analysed within the range of 1610–1710 cm^{-1}. First, as seen in (Fig. 5A), we imaged the maps at specific wavenumbers: 1600 cm^{-1}, indicative of PS-specific vibrations, and 1630 cm^{-1}, associated with β-sheet structures. Both maps were normalized to 1658 cm^{-1}, corresponding to total protein content (Fig. 5A). The comparison of spectral maps from PS-exposed and unexposed N2Aswe cells corresponding to specific frequencies revealed the intracellular presence and distribution of PS and β-sheet content. Notably, PS-exposed cells (N2Aswe + PS) exhibited a significant increase in the 1630 cm^{-1} signal (purple arrow) compared to control cells (grey arrow). These visualizations suggest elevated β-sheet levels in the presence of PS.

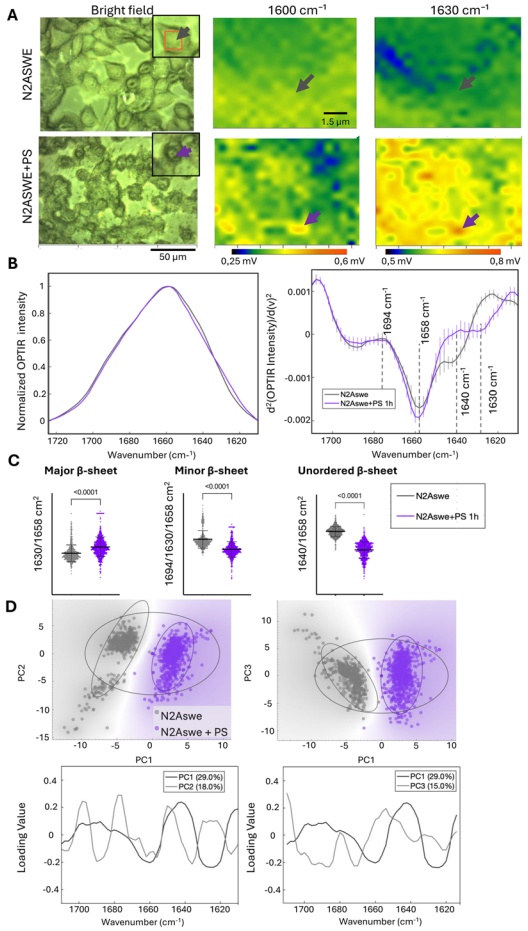

Fig. 5 PS-induced changes in β-sheet structures in an AD cellular model. (A) Bright-field image and hyperspectral O-PTIR maps of N2Aswe cells exposed or unexposed to PS, acquired at 1600 cm^{-1} (PS-specific signal), 1630 cm^{-1} (β-sheet content), normalized to 1658 cm^{-1} (total protein/α-helices). PS-exposed cells showed increased intensity at 1630 cm^{-1} (purple arrow) compared to non-exposed control (grey arrow). Inset: Magnified view of the demarcated cellular region used for spectral analysis. (B and C) Quantification of secondary structure components from second-derivative spectra of the amide I region. Ratios were calculated between 1630 cm^{-1} and 1658 cm^{-1} (total β-sheets) and 1694 cm^{-1} and 1658/1630 cm^{-1} (antiparallel β-sheets). (D) Principal component analysis (PCA) of amide I spectra (1610–1710 cm^{-1}) showing clear separation between PS-exposed and control N2Aswe cells. PCA loading plots indicated that wavenumbers corresponding to β-sheet structures contributed most strongly to group differentiation (data derived from n = 5 (control) and n = 6 (PS-exposed) individual cells, totaling >4000 spectra). Statistical significance determined by Mann–Whitney U test.

To quantify the relationship between PS exposure and elevated β-sheet structures in N2Aswe cells, we calculated the intensity ratios of secondary derivatives of amide I band positions, which enhances the resolution of overlapping spectral components (Fig. 5B and C and Table 1). This approach revealed that exposure to 480 µg mL^{-1} PS for 24 h induced marked changes in the β-sheet content of N2Aswe cells. The total β-sheet level was assessed by calculating the intensity ratio of the 1630 cm^{-1} band relative to the 1658 cm^{-1} band. Antiparallel β-sheet structures, indicated by the 1694 cm^{-1} band, were quantified by their intensity ratios relative to both 1658 cm^{-1} and 1630 cm^{-1}.

Likewise, unordered β-sheet structures at 1640 cm^{-1} were evaluated by calculating their intensity ratios relative to 1658 cm^{-1}. This approach normalizes β-sheet subtypes to both overall protein levels and total β-sheet content, providing a more detailed assessment of structural changes induced by PS exposure. This analysis confirmed that PS exposure results in an increase in β-sheet-rich content but a decrease of antiparallel and unordered β-sheet structures, indicating a reorganization of protein conformation in response to PS exposure. According to Barth,[29] specific amide I band positions reflect distinct β-sheet configurations and their hydrogen bonding environments.

The observed reduction in minor β-sheets implies a shift toward more aggregated or fibrillar β-sheet forms. These structural rearrangements may compromise protein folding fidelity, potentially disrupting cellular homeostasis. Proper folding is critical for protein stability and function, and early conformational changes, such as those observed here, are key events in the pathogenesis of protein misfolding diseases like AD.

To ensure statistical robustness beyond the cell count, we analysed a comprehensive dataset of over 4000 individual high-resolution spectra extracted from the hyperspectral maps. This massive spectral library allowed us to apply PCA to the spectra (Fig. 5D). PCA is a multivariate statistical tool that reduces complex spectral data into orthogonal components (principal components), enabling the identification of wavenumbers that contribute most significantly to differences between groups.[50] This method facilitates the identification of underlying patterns and clustering based on spectral similarities. In our analysis, the first four components accounted for 70% of the total variance (Fig. 5D and S4).

The PCA score plot clearly showed a distinct separation between PS-exposed and control in N2Aswe cell groups. It confirms that PS exposure induces systematic and quantifiable changes in the protein structure. The corresponding loading plots indicated that the wavenumbers contributing most strongly to group separation were those associated with β-sheet structural elements, further supporting our spectral interpretation.

Our findings indicate that exposure to PS can disrupt protein folding and stability by promoting β-sheet-rich conformations that are prone to aggregation. This structural shift may reflect an early step in pathological protein misfolding, which can affect cellular function. Given the wide presence of MNPs in the environment, it is crucial to determine whether similar protein-structural effects are triggered by other plastic types. Further investigation is needed to uncover the specific molecular mechanisms underlying PS interactions with β-sheet-containing proteins and to assess the long-term consequences of these interactions on human health.

Taken together, these data indicate that PS exposure contributes to intracellular protein aggregation, which consequently leads to metabolic dysregulation. These results align with studies demonstrating that MNPs can induce protein misfolding,[51,52] impair metabolic pathways,[9] and reduce cell viability.[53] Such disruptions to proteostasis and energy balance are well-established drivers of disease progression in neurodegeneration, cardiovascular disorders, and cancer.[6,8,54] These disease-related processes are often driven by mechanisms such as increased oxidative stress, dysfunction of the protein quality control system, and long-term alterations in cellular metabolism.[55–59] Therefore, understanding how environmental contaminants like PS affect protein structure at the molecular level is crucial for a better understanding of nanoplastics' potential role in AD and their impact on human health.

Discussion

The initial objective in understanding the biological impact of polystyrene (PS) nanoplastics was to assess the particle's behaviour within the biological medium. We utilized commercially standardized 0.2 μm polystyrene beads (Sigma-Aldrich), a model widely established in nanotoxicology research. Previous physicochemical characterization of these specific particles in serum-supplemented medium (DMEM with FBS) consistently reports the formation of a biomolecule corona. This is evidenced by a distinct zeta potential shift: while values in water are typically observed at approximately −45 mV, incubation in complete medium consistently shifts these values toward a stabilized range of −20 to −13 mV.[60–63] However, while zeta potential infers surface interaction *via* charge alteration, we employed small-angle X-ray scattering to directly quantify the physical dimensions of this complex. Our SAXS measurements (Fig. 2D) confirmed a quantifiable increase in the radius of gyration (R_g), providing definitive structural verification of the Aβ coating in a physiological environment. This established profile indicates that serum proteins adsorb onto the PS surface, providing steric stabilization that facilitates cellular uptake *via* endocytosis.[61]

Our imaging data confirm this behaviour in our system, showing that PS particles remained dispersed as distinct puncta within the cytoplasm rather than forming large extracellular agglomerates. Consequently, the internalized PS surface acts as a reactive interface available for interaction with intracellular proteins, supporting our core hypothesis that the particle facilitates pathological protein processes.[52,62]

Our investigation demonstrated that the presence of PS nanoplastics significantly promote amyloid protein aggregation. Through multi-modal analysis, including fluorescence microscopy, TEM, SEM, and SAXS, we observed that co-incubation of recombinant Aβ(1–42) with PS resulted in the formation of larger, more complex aggregated structures compared to Aβ(1–42) alone. O-PTIR spectroscopy provided critical molecular evidence, confirming the co-presence and interaction of PS (1600 cm^{-1}) and Aβ(1–42) (1632 cm^{-1}) within the same aggregate area. This evidence strongly supports the model that the PS nanoplastics act as a nucleation scaffold or heterogeneous catalyst, accelerating the initial kinetic steps of Aβ aggregation.[19]

While the *in vitro* data confirmed strong aggregation, rigorous environmental toxicology requires validation of the exposure dose. The WST-1 assay (Fig. S2B) indicated a significant, dose-dependent decrease in metabolic activity, suggesting initial cellular stress. To definitively validate whether this metabolic impairment progressed to irreversible cell death, we performed the LDH cytotoxicity assay (Fig. S2C). The results conclusively demonstrated that the PS concentrations used are sublethal in both N2Awt and N2Aswe cells at 24 h, with LDH release remaining at basal levels. Crucially, in the N2Awt cells, neither 10 mM Aβ(1–42) alone nor the co-exposure of PS + Aβ(1–42) at the highest dose induced acute cell death. This validates our experimental approach: the doses are suitable for investigating sublethal mechanistic changes that precede acute toxicity.[12,56,64]

The observed metabolic decline is underpinned by significant structural and cellular dysfunction. The co-localization of PS with the lysosomal marker Lamp1 confirms lysosomal uptake and engagement.[63] The failure to clear these aggregates, particularly in the N2Aswe cells, is indicated by the subsequent increase in caspase-3, suggesting that the PS–Aβ complex initiates apoptotic signalling. Notably, these lipidomic alterations mirror the specific metabolic deviations observed in human AD brains, suggesting that nanoplastic exposure may mimic or accelerate intrinsic pathological pathways. The O-PTIR data provided the critical structural link. By focusing on the N2Aswe model, which offers a high density of amyloid targets, we were able to resolve that PS exposure induced marked structural alterations in cellular proteins, specifically evidenced by a significant increase in the 1630 cm^{-1} β-sheet signal and a reduction in antiparallel and unordered structures. This conformational rearrangement supports the hypothesis that the PS surface templates a shift toward highly aggregated, pathogenic Aβ forms. This structural shift, confirmed by principal component analysis (PCA) clustering, validates that PS promotes pathological protein misfolding, which, combined with metabolic failure, drives toxicity.[65]

An important aspect emerging from our data is that the effect of polystyrene (PS) nanoplastics on Aβ is not limited to a simple increase in aggregate mass but involves qualitative conformational remodelling. In contrast to the enhanced β-sheet signal observed in the N2Aswe model under high amyloid load, the experiments performed in cells exposed to exogenous Aβ(1–42) revealed a reduction of the characteristic β-sheet shoulder (~1630–1635 cm^{-1}) in the presence of nanoplastics. This apparent discrepancy likely reflects context-dependent structural templating.

In a system with abundant intracellular Aβ targets (N2Aswe), the PS surface may stabilize and amplify

β-sheet-rich assemblies. In contrast, during early-stage aggregation of externally supplied Aβ, the same surface may interfere with fibril maturation, promoting alternative conformers or less ordered assemblies. Such surface-driven conformational plasticity is consistent with heterogeneous nucleation theory, where nanoscale interfaces alter the energy landscape of protein folding and misfolding. Thus, PS nanoplastics should be considered dynamic catalytic interfaces that modulate amyloid structure in a context-dependent manner. This mechanistic flexibility may be particularly relevant *in vivo*, where varying protein concentrations, lipid composition, and intracellular compartmentalization could determine whether nanoplastics accelerate fibrillization, stabilize toxic oligomers, or redirect aggregation pathways altogether.

We acknowledge that the PS concentrations utilized (120–480 μg mL^{-1}), while confirmed to be sublethal by our LDH analysis, are higher than current estimates of environmental exposure. However, these concentrations were specifically selected to align with the experimental framework established by Yang *et al.* (2022),[32] ensuring a comparable toxicological baseline. While their work identified that these doses induce ROS-mediated neuronal apoptosis, our study advances this finding by identifying the upstream molecular trigger: the surface-catalysed misfolding of amyloid proteins. The use of these established doses was technically requisite for O-PTIR analysis, the high signal-to-noise ratio allowed us to spectrally confirm the co-localization of PS and amyloid aggregates *in situ*, a mechanistic confirmation that would be unresolvable at trace environmental levels. Consequently, this study serves as a mechanistic proof of concept; identifying the specific surface interactions that drive toxicity, which can now be targeted in future chronic exposure studies. Second, while the use of commercially standardized, pristine PS beads allows for reproducible physicochemical characterization, it does not fully capture the complexity of weathered, irregular microplastics found in nature, which may possess different surface chemistries and protein corona profiles. However, since the observed mechanism is driven by surface hydrophobicity and protein corona formation, we posit that this 'catalytic scaffold' effect is likely a shared feature across other hydrophobic polymers like polyethylene and polypropylene, broadening the potential environmental implications. Future work utilizing aged or environmentally sampled nanoplastics in complex co-culture models will be essential to further validate the toxicological pathway identified here.

Limitations of the study: first, although the N2a-APPsw cell line stably expresses the human APP gene carrying the Swedish mutation (K670N/M671L), effectively recapitulating clinically relevant human Aβ production, the host cells are of murine neuroblastoma origin. Consequently, this model does not fully recapitulate the complex genetic and physiological environment of primary human neurons. Future studies utilizing human iPSCs or organoid models would further enhance translational relevance.

Additionally, we utilized uniform polystyrene beads to standardize surface area and chemistry. While real-world environmental exposures involve heterogeneous mixtures, establishing the molecular mechanism of the pure polymer core is a prerequisite to interpreting complex environmental interactions.

Furthermore, the exposure concentrations and durations used here represent an accelerated acute model to isolate specific molecular mechanisms; this differs from the chronic, low-dose bioaccumulation patterns likely occurring in human neural tissues over decades. Finally, while our spectral analysis focused on Aβ-specific signatures, it is important to acknowledge that the physical burden of intracellular nanoplastics likely challenges broader cellular proteostasis. Some of the observed metabolic disruptions may therefore reflect a generalized stress response rather than exclusively Aβ-mediated pathology.

Conclusion

In conclusion, by employing sub-diffraction O-PTIR imaging, this study provides direct spectroscopic validation that polystyrene surfaces act as catalytic scaffolds for amyloid misfolding *in situ*. We demonstrated that internalized polystyrene particles recruit Aβ peptides, driving a distinct structural reorganization toward β-sheet-rich conformations within the endolysosomal pathway.

This physical interaction is accompanied by significant metabolic disruptions, specifically lipid processing defects, which occur even at sublethal concentrations. Collectively, these data identify a specific molecular mechanism by which accumulating synthetic particles can exacerbate the pathological hallmarks of AD, highlighting the neurotoxic potential of nanoplastic bioaccumulation.

Author contributions

Iran Augusto Neves da Silva contributed to conceptualization, methodology, formal analysis, investigation, data curation, writing – original draft preparation, project administration, and funding acquisition. Agnes Paulus contributed to conceptualization, methodology, formal analysis, investigation, data curation, writing – review & editing, and project administration. Valeriia Skoryk contributed to methodology, formal analysis, investigation, data curation, and writing – review & editing. Kar-Yan Su contributed to methodology, investigation, and writing – review & editing. Fátima Herranz-Trillo contributed to investigation and writing – review & editing. Klementieva Oxana contributed to conceptualization, methodology, investigation, data curation, writing – review & editing, project administration, resources, and funding acquisition. All authors have read and agreed to the published version of the manuscript.

Conflicts of interest

There are no conflicts to declare.

Abbreviations

MNPs	Microplastics and nanoplastics
MPs	Microplastics (<5 mm)
NPs	Nanoplastics (<100 nm)
PS	Polystyrene
AD	Alzheimer's disease
O-PTIR	Optical photothermal infrared
N2Awt	N2A wild type
N2Aswe	N2A cell line stably transfected with human APP carrying the Swedish mutation
DMEM	Dulbecco's modified Eagle medium
Opti-MEM	A cell culture medium
FBS	Fetal bovine serum
p/s	Penicillin/streptomycin
CO_2	Carbon dioxide
WST-1	Water-soluble tetrazolium-1
UV-vis	Ultraviolet-visible
IR	Infrared
QCL	Quantum cascade laser
TEM	Transmission electron microscopy
SEM	Scanning electron microscopy
DAPI	365/415 nm dye
CY5	580/605 nm dye
APP	Amyloid precursor protein
Aβ	Amyloid beta
HEWL	Hen egg-white lysozyme
LPS	Lipopolysaccharide
SAXS	Small angle X-ray scattering
R_g	Radius of gyration
WT	Wild type cells (N2Awt)
SW	Swedish mutation cells (N2Aswe)
PCA	Principal component analysis

Data availability

Raw O-PTIR spectral and SAXS data and imaging datasets generated during the current study are available from the corresponding author on reasonable request.

Supplementary information (SI): the SI provides extended O PTIR spectral data and pair distance distribution profiles for Aβ and PS. It features dose dependent cell viability and cytotoxicity data including WST 1 and LDH assays. It further includes baseline quantifications for Caspase 3 and LAMP1 with co localization percentages, and in depth Principal Component Analysis of cellular O PTIR spectra confirming structural alterations. See DOI: https://doi.org/10.1039/d5en01181g.

Acknowledgements

We acknowledge the Microscopy for Biosciences (M-bio) Facility at the Faculty of Science, Department of Biology, Lund University. We also acknowledge the MAX IV Laboratory for beamtime on the CoSAXS beamline under proposal 20230450. Research conducted at MAX IV, a Swedish national user facility, is supported by the Swedish Research Council (grant number 2018-07152), Vinnova (grant number 2018-04969), Formas (grant number 2019-02496), Strategic Research Environment MultiPark and Nanolund (Multidisciplinary research on Parkinson's disease), The Brain Foundation (FO2022-0329) and The Royal Physiographic Society of Lund (grant numbers F 2024/1892 and F 2024/1891). We also acknowledge the Swedish Foundation for Strategic Research (grant number UKR24-0022), Crafoordska stiftelsen (grant number 20250747), and Olle Engkvists 220-0182 Forskningsprojekt.

Notes and references

1 B. Jiang, A. E. Kauffman, L. Li, W. McFee, B. Cai and J. Weinstein, *et al.*, Health impacts of environmental contamination of micro-and nanoplastics: a review, *Environ. Health Prev. Med.*, 2020, **25**, 1–15.
2 O. S. Alimi, J. Farner Budarz, L. M. Hernandez and N. Tufenkji, Microplastics and Nanoplastics in Aquatic Environments: Aggregation, Deposition, and Enhanced Contaminant Transport, *Environ. Sci. Technol.*, 2018, **52**(4), 1704–1724.
3 A. L. Andrady and M. A. Neal, Applications and societal benefits of plastics, *Philos. Trans. R. Soc., B*, 2009, **364**(1526), 1977–1984.
4 E. C. Ebere, V. A. Wirnkor and V. E. Ngozi, Uptake of microplastics by plant: a reason to worry or to be happy?, *World Sci. News*, 2019(131), 256–267.
5 C. E. Enyoh, L. Shafea, A. W. Verla, E. N. Verla, W. Qingyue and T. Chowdhury, *et al.*, Microplastics exposure routes and toxicity studies to ecosystems: an overview, *Environ. Anal. Health Toxicol.*, 2020, **35**(1), e2020004.
6 J. C. Prata, J. P. da Costa, I. Lopes, A. C. Duarte and T. Rocha-Santos, Environmental exposure to microplastics: An overview on possible human health effects, *Sci. Total Environ.*, 2020, **702**, 134455.
7 L. M. Hernandez, E. G. Xu, H. C. Larsson, R. Tahara, V. B. Maisuria and N. Tufenkji, Plastic teabags release billions of microparticles and nanoparticles into tea, *Environ. Sci. Technol.*, 2019, **53**(21), 12300–12310.
8 S. Urli, F. Corte Pause, M. Crociati, A. Baufeld, M. Monaci and G. Stradaioli, Impact of Microplastics and Nanoplastics on Livestock Health: An Emerging Risk for Reproductive Efficiency, *Animals*, 2023, **13**(7), 1132.
9 A. J. Nihart, M. A. Garcia, E. El Hayek, R. Liu, M. Olewine and J. D. Kingston, *et al.*, Bioaccumulation of microplastics in decedent human brains, *Nat. Med.*, 2025, 1–6.
10 G.-f. Chen, T.-h. Xu, Y. Yan, Y.-r. Zhou, Y. Jiang and K. Melcher, *et al.*, Amyloid beta: structure, biology and structure-based therapeutic development, *Acta Pharmacol. Sin.*, 2017, **38**(9), 1205–1235.
11 J. Windheim, L. Colombo, N. C. Battajni, L. Russo, A. Cagnotto and L. Diomede, *et al.*, Micro-and nanoplastics' effects on protein folding and amyloidosis, *Int. J. Mol. Sci.*, 2022, **23**(18), 10329.
12 S. Shan, Y. Zhang, H. Zhao, T. Zeng and X. Zhao, Polystyrene nanoplastics penetrate across the blood-brain barrier and induce activation of microglia in the brain of mice, *Chemosphere*, 2022, **298**, 134261.

13 Y. Wang, G. Huang, X. Liang, N. Andrikopoulos, H. Tang and F. Ding, *et al.*, Microglial clearance of Alzheimer's amyloid-beta obstructed by nanoplastics, *Environ. Sci.: Nano*, 2025, **12**, 3247–3260.
14 X. Liang, Y. Wang, N. Andrikopoulos, P. C. Ke and Y. Li, Dysfunctional digestive tract highlights the metabolic hallmarks of nanoplastic-exacerbated Parkinson's pathology, *npj Parkinson's Dis.*, 2025, **11**(1), 300.
15 N. Bashirova, F. Schölzel, D. Hornig, H. A. Scheidt, M. Krueger and G. Salvan, *et al.*, The Effect of Polyethylene Terephthalate Nanoplastics on Amyloid-β Peptide Fibrillation, *Molecules*, 2025, **30**(7), 1432.
16 X. Gou, Y. Fu, J. Li, J. Xiang, M. Yang and Y. Zhang, Impact of nanoplastics on Alzheimer's disease: Enhanced amyloid-β peptide aggregation and augmented neurotoxicity, *J. Hazard. Mater.*, 2024, **465**, 133518.
17 M. Mahmoudi, H. R. Kalhor, S. Laurent and I. Lynch, Protein fibrillation and nanoparticle interactions: opportunities and challenges, *Nanoscale*, 2013, **5**(7), 2570–2588.
18 K. Hensley, J. Carney, M. Mattson, M. Aksenova, M. Harris and J. Wu, *et al.*, A model for beta-amyloid aggregation and neurotoxicity based on free radical generation by the peptide: relevance to Alzheimer disease, *Proc. Natl. Acad. Sci. U. S. A.*, 1994, **91**(8), 3270–3274.
19 C. Cabaleiro-Lago, F. Quinlan-Pluck, I. Lynch, K. A. Dawson and S. Linse, Dual effect of amino modified polystyrene nanoparticles on amyloid β protein fibrillation, *ACS Chem. Neurosci.*, 2010, **1**(4), 279–287.
20 A. Salminen, A. Kauppinen and K. Kaarniranta, Emerging role of NF-κB signaling in the induction of senescence-associated secretory phenotype (SASP), *Cell. Signalling*, 2012, **24**(4), 835–845.
21 M. Varela-Eirín and M. Demaria, Cellular senescence, *Curr. Biol.*, 2022, **32**(10), R448–R452.
22 D. Yang, J. Zhu, X. Zhou, D. Pan, S. Nan and R. Yin, *et al.*, Polystyrene micro-and nano-particle coexposure injures fetal thalamus by inducing ROS-mediated cell apoptosis, *Environ. Int.*, 2022, **166**, 107362.
23 Q. Yang, H. Dai, Y. Cheng, B. Wang, J. Xu and Y. Zhang, *et al.*, Oral feeding of nanoplastics affects brain function of mice by inducing macrophage IL-1 signal in the intestine, *Cell Rep.*, 2023, **42**(4), 112346.
24 D. J. Selkoe, Alzheimer's disease results from the cerebral accumulation and cytotoxicity of amyloid ß-protein, *J. Alzheimer's Dis.*, 2001, **3**(1), 75–80.
25 G. K. Gouras, T. T. Olsson and O. Hansson, β-Amyloid peptides and amyloid plaques in Alzheimer's disease, *Neurotherapeutics*, 2015, **12**(1), 3–11.
26 N. Gvazava, S. C. Konings, E. Cepeda-Prado, V. Skoryk, C. H. Umeano and J. Dong, *et al.*, Label-free high-resolution photothermal optical infrared spectroscopy for spatiotemporal chemical analysis in fresh, hydrated living tissues and embryos, *J. Am. Chem. Soc.*, 2023, **145**(45), 24796–24808.
27 C. B. Prater, M. Kansiz and J.-X. Cheng, A tutorial on optical photothermal infrared (O-PTIR) microscopy, *APL Photonics*, 2024, **9**(9), 091101.
28 J.-X. Cheng and X. S. Xie, *Coherent anti-Stokes Raman scattering microscopy: instrumentation, theory, and applications*, ACS Publications, 2004, pp. 827–840.
29 A. Barth, Infrared spectroscopy of proteins, *Biochim. Biophys. Acta, Bioenerg.*, 2007, **1767**(9), 1073–1101.
30 E. Cerf, R. Sarroukh, S. Tamamizu-Kato, L. Breydo, S. Derclaye and Y. F. Dufrêne, *et al.*, Antiparallel β-sheet: a signature structure of the oligomeric amyloid β-peptide, *Biochem. J.*, 2009, **421**(3), 415–423.
31 G. Thinakaran, D. B. Teplow, R. Siman, B. Greenberg and S. S. Sisodia, Metabolism of the "Swedish" amyloid precursor protein variant in neuro2a (N2a) cells: evidence that cleavage at the "β-secretase" site occurs in the Golgi apparatus (*), *J. Biol. Chem.*, 1996, **271**(16), 9390–9397.
32 D. Yang, J. Zhu, X. Zhou, D. Pan, S. Nan and R. Yin, *et al.*, Polystyrene micro- and nano-particle coexposure injures fetal thalamus by inducing ROS-mediated cell apoptosis, *Environ. Int.*, 2022, **166**, 107362.
33 I. A. Da Silva, N. Gvazava, I. Putra Wendi, R. Guinea, F. García Giménez and J. Stegmayr, *et al.*, Formalin-free fixation and xylene-free tissue processing preserves cell-hydrogel interactions for histological evaluation of 3D calcium alginate tissue engineered constructs, *Front. Biomater. Sci.*, 2023, **2**, 1155919.
34 D. Ami, P. Mereghetti and A. Natalello, Contribution of infrared spectroscopy to the understanding of amyloid protein aggregation in complex systems, *Front. Mol. Biosci.*, 2022, **9**, 822852.
35 C. F. Geraldes, Introduction to infrared and Raman-based biomedical molecular imaging and comparison with other modalities, *Molecules*, 2020, **25**(23), 5547.
36 A. Mitchell and H. Rubinsztein-Dunlop, AOS Australian Conference on Optical Fibre Technology (ACOFT) and Australian Conference on Optics, Lasers, and Spectroscopy (ACOLS) 2019, in *Proc. of SPIE*, 2019, vol. 11200, p. 1120001-1.
37 M. Kansiz, C. Prater, E. Dillon, M. Lo, J. Anderson and C. Marcott, *et al.*, Optical photothermal infrared microspectroscopy with simultaneous Raman-a new non-contact failure analysis technique for identification of <10 μm organic contamination in the hard drive and other electronics industries, *Microsc. Today*, 2020, **28**(3), 26–36.
38 D. Zhang, C. Li, C. Zhang, M. N. Slipchenko, G. Eakins and J.-X. Cheng, Depth-resolved mid-infrared photothermal imaging of living cells and organisms with submicrometer spatial resolution, *Sci. Adv.*, 2016, **2**(9), e1600521.
39 J. Demšar and B. Zupan, Hands-on training about data clustering with orange data mining toolbox, *PLoS Comput. Biol.*, 2024, **20**(12), e1012574.
40 D. Baghel, A. P. de Oliveira, S. Satyarthy, W. E. Chase, S. Banerjee and A. Ghosh, Chapter Six - Structural characterization of amyloid aggregates with spatially resolved infrared spectroscopy, in *Methods in Enzymology*, ed. I. V. Korendovych, Academic Press, 2024, vol. 697, pp. 113–150.
41 M. P. Confer, B. M. Holcombe, A. G. Foes, J. M. Holmquist, S. C. Walker and S. Deb, *et al.*, Label-free infrared spectroscopic imaging reveals heterogeneity of β-sheet

aggregates in Alzheimer's disease, *J. Phys. Chem. Lett.*, 2021, **12**(39), 9662–9671.
42 B. Holcombe, A. Foes, S. Banerjee, K. Yeh, S.-H. J. Wang and R. Bhargava, *et al.*, Intermediate Antiparallel β Structure in Amyloid β Plaques Revealed by Infrared Spectroscopic Imaging, *ACS Chem. Neurosci.*, 2023, **14**(20), 3794–3803.
43 Z. Ganim, H. S. Chung, A. W. Smith, L. P. DeFlores, K. C. Jones and A. Tokmakoff, Amide I two-dimensional infrared spectroscopy of proteins, *Acc. Chem. Res.*, 2008, **41**(3), 432–441.
44 K. Duswald, V. Pichler, V. Kopatz, T. Limberger, V. Karl and D. Wimberger, *et al.*, Detection of Unlabeled Micro- and Nanoplastics in Unstained Tissue with Optical Photothermal Infrared Spectroscopy, *bioRxiv*, 2024, preprint, DOI: 10.1101/2024.11.11.622943.
45 M. V. Petoukhov, P. V. Konarev, A. G. Kikhney and D. I. Svergun, ATSAS 2.1-towards automated and web-supported small-angle scattering data analysis, *Appl. Crystallogr.*, 2007, **40**(s1), s223–s228.
46 K. Manalastas-Cantos, P. V. Konarev, N. R. Hajizadeh, A. G. Kikhney, M. V. Petoukhov and D. S. Molodenskiy, *et al.*, ATSAS 3.0: expanded functionality and new tools for small-angle scattering data analysis, *Appl. Crystallogr.*, 2021, **54**(1), 343–355.
47 P. Painter, M. Sobkowiak and Y. Park, Vibrational relaxation in atactic polystyrene: an infrared spectroscopic study, *Macromolecules*, 2007, **40**(5), 1730–1737.
48 E. G. Chatzi, O. Kammona, A. Kentepozidou and C. Kiparissides, Infrared spectra and compositional analysis of styrene/2-ethylhexyl acrylate copolymers, *Macromol. Chem. Phys.*, 1997, **198**(8), 2409–2420.
49 X. Gou, Y. Fu, J. Li, J. Xiang, M. Yang and Y. Zhang, Impact of nanoplastics on Alzheimer's disease: Enhanced amyloid-β peptide aggregation and augmented neurotoxicity, *J. Hazard. Mater.*, 2024, **465**, 133518.
50 D. Groth, S. Hartmann, S. Klie and J. Selbig, Principal components analysis, *Computational Toxicology: Volume II*, 2013, pp. 527–547.
51 E. L. Bearer, M. A. Garcia, N. Adolphi and M. J. Campen, White matter hyperintensities and microplastics, *bioRxiv*, 2024, preprint, DOI: 10.1101/2024.11.26.625277.
52 Y. Chen, Q. Liu, S. Mi, S. Yuan, H. Yu and Y. Guo, *et al.*, The impact of modified polystyrene on lysozyme fibrillation studied by surface-enhanced Raman spectroscopy (SERS), *Int. J. Biol. Macromol.*, 2023, **242**, 124937.
53 K. Murali, Y. Li, K. Demeter, Z. Környei and E. Madarász, Uptake and bio-reactivity of polystyrene nanoparticles is affected by surface modifications, ageing and LPS adsorption: in vitro studies on neural tissue cells, *Nanoscale*, 2015, **7**(9), 4199–4210.
54 S. Rist, B. C. Almroth, N. B. Hartmann and T. M. Karlsson, A critical perspective on early communications concerning human health aspects of microplastics, *Sci. Total Environ.*, 2018, **626**, 720–726.
55 L. Lu, Z. Wan, T. Luo, Z. Fu and Y. Jin, Polystyrene microplastics induce gut microbiota dysbiosis and hepatic lipid metabolism disorder in mice, *Sci. Total Environ.*, 2018, **631**, 449–458.
56 M. Hu and D. Palić, Micro-and nano-plastics activation of oxidative and inflammatory adverse outcome pathways, *Redox Biol.*, 2020, **37**, 101620.
57 P. M. Gopinath, K. S. Twayana, P. Ravanan, J. Thomas, A. Mukherjee and D. F. Jenkins, *et al.*, Prospects on the nano-plastic particles internalization and induction of cellular response in human keratinocytes, *Part. Fibre Toxicol.*, 2021, **18**(1), 1–24.
58 M. Ehsanifar, Z. Montazeri, M. A. Taheri, M. Rafati, M. Behjati and M. Karimian, Hippocampal inflammation and oxidative stress following exposure to diesel exhaust nanoparticles in male and female mice, *Neurochem. Int.*, 2021, **145**, 104989.
59 H. Zhang, W. Jiao, H. Cui, Q. Sun and H. Fan, Combined exposure of alumina nanoparticles and chronic stress exacerbates hippocampal neuronal ferroptosis via activating IFN-γ/ASK1/JNK signaling pathway in rats, *J. Hazard. Mater.*, 2021, **411**, 125179.
60 Y. Hou, S. Tu, X. Zhao, G. Li, N. Li and A. Zou, An integrative method for evaluating the biological effects of nanoparticle-protein corona, *Biochim. Biophys. Acta, Gen. Subj.*, 2023, **1867**(3), 130300.
61 S. Han, R. da Costa Marques, J. Simon, A. Kaltbeitzel, K. Koynov and K. Landfester, *et al.*, Endosomal sorting results in a selective separation of the protein corona from nanoparticles, *Nat. Commun.*, 2023, **14**(1), 295.
62 K. Tallec, O. Blard, C. González-Fernández, G. Brotons, M. Berchel and P. Soudant, *et al.*, Surface functionalization determines behavior of nanoplastic solutions in model aquatic environments, *Chemosphere*, 2019, **225**, 639–646.
63 C. Mota, A. M. Araújo, M. Enea, E. Pereira, A. Reis-Mendes and R. Fernandes, *et al.*, Are all nanoplastics equally neurotoxic? Influence of size and surface functionalization on the toxicity of polystyrene nanoplastics in human neuronal cells, *Environ. Pollut.*, 2026, **390**, 127445.
64 S. Ghosal, S. Bag and S. Bhowmik, Insights into the binding interactions between microplastics and human α-synuclein protein by multispectroscopic investigations and amyloidogenic oligomer formation, *J. Phys. Chem. Lett.*, 2024, **15**(25), 6560–6567.
65 O. Klementieva, C. Sandt, I. Martinsson, M. Kansiz, G. K. Gouras and F. Borondics, Super-Resolution Infrared Imaging of Polymorphic Amyloid Aggregates Directly in Neurons, *Adv. Sci.*, 2020, **7**(6), 1903004.
66 I. Silva, O-PTIR spectra of polystyrene, *BioRender*, 2025.
67 I. da Silva, The experimental timeline is schematically represented AB + PS, *BioRender*, 2025.